Unified Prandtl number scaling for start-up and fully developed natural-convection boundary layers for both Pr $\gtrsim$ 1 and Pr $\lesssim$ 1 fluids with isothermal heating

Wenxian Lin[1,2,*] and S. W. Armfield[3]

[1]*Solar Energy Research Institute, Yunnan Normal University, Kunming, Yunnan 650092, People's Republic of China*

[2]*School of Engineering, James Cook University, Townsville, QLD 4811, Australia*

[3]*School of Aerospace, Mechanical and Mechatronic Engineering, University of Sydney, NSW 2006, Australia*

(Received 24 April 2012; published 14 December 2012)

Recent studies have used scaling analysis to obtain simple power-law relations that accurately predict the Prandtl (Pr) number dependency of natural-convection boundary layers subjected to both isothermal and ramped heating conditions, when Pr > 1. The analysis used in those studies cannot be extended to Pr < 1 fluids, and it is not clear at present whether such simple scaling relations can be developed for Pr < 1 fluids. In the present study, the Pr > 1 scalings are shown to perform well for the start-up stage of the Pr < 1 flow, but not for the fully developed flow. The Pr > 1 scalings are modified to provide unified Prandtl number scalings for fully developed natural-convection boundary layers for both Pr $\gtrsim$ 1 and Pr $\lesssim$ 1, with the unknown powers obtained empirically via direct numerical simulation. The modified scalings are shown to perform well for the fully developed flow, with the exception being the prediction of the inner viscous boundary-layer thickness.

DOI: 10.1103/PhysRevE.86.066312 PACS number(s): 44.25.+f, 47.55.P−, 44.20.+b, 47.15.Cb

I. INTRODUCTION

Due to its fundamental and practical significance, natural-convection boundary-layer flow is a classic problem in fluid mechanics and heat transfer and has been the subject of extensive experimental, analytical, and numerical studies. Earlier studies had focused on the experimental and analytical explorations of the steady-state behavior of the flow, particularly that in a rectangular cavity with differentially heated sidewalls. These studies have been reviewed by Catton [1], Ostrach [2], Gebhart *et al.* [3], Hyun [4], and more recently by regular literature reviews in heat transfer (see, e.g., Goldstein *et al.* [5] and Shih *et al.* [6,7]).

More recent studies on natural-convection boundary layers have focused on their transient flow behavior, which is also of fundamental interest and practical importance. Patterson and Imberger [8] carried out a pioneering scaling analysis on transient natural-convection boundary-layer flow in the context of a two-dimensional rectangular cavity when its opposing two vertical sidewalls are impulsively heated and cooled by an equal amount. They devised a classification of the flow development through several transient flow regimes to one of three steady-state types of flow in terms of the Rayleigh number Ra, the Prandtl number Pr, and the aspect ratio of the cavity, A. This study has led to extensive subsequent investigations on many aspects of transient natural-convection boundary layers under various flow configurations and conditions through scaling analysis, numerical simulations, and experiments.

Lin and Armfield [9,10] obtained scalings by following a similar scaling analysis to that of Patterson and Imberger [8] for the development of unsteady natural convection in rectangular and vertical circular containers for fluids with Pr > 1. They identified three main development stages for the flow, i.e., the growth of the vertical thermal boundary layers on the sidewalls, the passage of the horizontal viscous intrusions, and the stratification of the flow core. They developed the scalings for the major parameters characterizing the flow, including the thermal boundary-layer thickness, the intrusion thickness, the rate of stratification, the time to attain full stratification, and the Nusselt number, in terms of Ra, Pr, and A, which were successfully verified and quantified by their direct numerical simulation results. Some of these scalings were verified by the study of Lira [11], who obtained scalings for the local Nusselt number for the laminar steady-state natural convection surrounding an isothermal vertical cylinder. Lin and Armfield [12] extended this scaling analysis to the long-term behavior of cooling fluids with Pr < 1 via natural convection in a vertical cylinder with an imposed constant lower temperature on the vertical sidewalls. In this case, they found that the flow is dominated by three distinct stages of development, i.e., the boundary-layer development stage adjacent to the sidewalls, the stratification stage, and the cooling-down stage. The first stage can be further divided into three substages, i.e., the start-up stage, the transitional stage, and the boundary-layer steady-state stage. For each development stage and substage, they obtained the scalings for the maximum velocity in the boundary layer, thermal and viscous boundary-layer thickness, local and overall Nusselt number, and times for full stratification and cooling-down, in terms of Ra, Pr, and A, which were again successfully verified and quantified by a series of direct numerical simulations. In the case of a rectangular container with an imposed constant lower temperature on the vertical sidewalls, Lin, Armfield, and Patterson [13] conducted a similar scaling analysis for the long-term behavior of cooling fluids with Pr < 1 via natural convection, and they obtained similar scalings for various parameters characterizing the flow behavior, which were also successfully verified and quantified by a series of direct numerical simulations. Armfield, Patterson, and Lin [14] considered the unsteady natural-convection boundary layer on an evenly heated semi-infinite plate with isoflux heating in ambient fluids with Pr > 1, and they developed scalings for the startup, transition, and full development of the natural-convection

*wenxian.lin@jcu.edu.au

boundary layer. The scalings they obtained describe the rate of growth of the boundary-layer velocity, temperature and thermal boundary-layer width, and the transition time and fully developed values for both neutral and stable linearly stratified ambient fluids. In particular, the scaling results indicate that at full development the stratified case will have a region of two-dimensional flow near the plate origin, while the remainder of the flow, far from the plate region, will be one-dimensional. This scaling analysis was later extended by Lin, Armfield, and Patterson [15] to the same case as that of Armfield *et al.* [14], but for fluids with $\mathrm{Pr} < 1$. They obtained significantly different scalings for the same parameters. They also found that oscillations are present at the transitional stage of the flow development. Kottke, Ferguson, and Fedorov [16] used the scaling analysis to provide scalings predicting heat transfer of combined convection and radiation problems in boundary-layer flows. They considered two limiting cases: the first one includes both forced- and natural-convection heat transfer components in conjunction with radiative heat transfer from a gray wall with a specified heat flux to a surrounding nonparticipating medium, and the second case includes forced-, natural-, and mixed-convection heat transfer components in conjunction with radiative heat transfer from a black wall with a specified temperature to an optically thick, gray, nonscattering medium. For the first case, they identified a dimensionless parameter to determine whether radiation or convection effects dominate, and they developed the scalings to estimate the wall temperature. For the second case, they found that a thermal mixing parameter can be introduced to determine the dominant mode of heat transfer, i.e., the importance of buoyancy effects in a forced-convection flow with thermal radiation, or, conversely, the importance of assisting flow in a free-convection–thermal radiation problem. Alloui, Vasseur, and Reggio [17] recently extended the scaling analysis to the natural-convection flow in a very tall vertical enclosure filled with nanofluids, and they obtained scalings for the boundary-layer thickness and the Nusselt number in terms of Ra, Pr, and the effective dynamic viscosity.

All the above-mentioned examples are for natural-convection boundary layers on vertical walls. There have been many studies on natural-convection boundary layers on inclined walls as well. For example, Saha and Khan [18] carried out a scaling analysis for the natural-convection boundary layer adjacent to an inclined semi-infinite plate subject to a noninstantaneous heating in the form of an imposed wall temperature which increases linearly up to a prescribed steady value over a prescribed time. They found that if the period of temperature growth on the wall is sufficiently long, the boundary layer reaches a quasisteady mode before the growth of the temperature is completed. In this mode, the thermal boundary layer at first grows in thickness and then contracts with increasing time. However, if the imposed wall temperature growth period is too short, the boundary layer develops differently, but after the wall temperature growth is completed the boundary layer develops as though the startup had been instantaneous. The steady-state values of the boundary layer for both cases are ultimately the same. They also obtained the scalings for the maximum velocity in the boundary layer, the time for the boundary layer to reach the quasisteady mode, and the thermal and viscous boundary-layer thickness.

Although the analytically derived scaling relations have been shown to correctly predict the Ra dependence under various flow conditions and configurations, as demonstrated by the studies mentioned above, it has also been shown that some of the scalings do not perform satisfactorily with the Pr variation. For example, the study by Lin *et al.* [13] reveals that there is a further dependence on Pr which is not fully captured by the standard scaling analysis as used in the above-mentioned studies. A recent study by Capobianchi and Aziz [19], who conducted a scaling analysis for natural-convection flow on a vertical plate under three different heating boundary conditions, i.e., at a constant surface temperature, a constant surface heat flux, and heating from the plate's back surface, for the entire range of Pr from zero to infinity, found that the scalings obtained for the Nusselt number are functions of $\mathrm{RaPr}/(1+\mathrm{Pr})$ raised to a power that depends on the boundary condition. For example, for the constant temperature and the constant heat flux boundary conditions, the scalings reduce to the asymptotic orders of magnitude for very large and very low Prandtl numbers reported in the literature, whereas for the case of plate heating from the opposing side the scalings are functions of $\mathrm{RaPr}/(1+\mathrm{Pr})$ raised to a power times a coefficient that is a function of RaPr, showing a further dependence on Pr. By taking into account the Pr variation in the scaling analysis, Lin *et al.* [20] and Patterson *et al.* [21] successfully addressed this problem and developed improved scalings for start-up and fully developed natural convection boundary layers for $\mathrm{Pr} > 1$ fluids under isothermal heating conditions and under ramp heating conditions, respectively. The major improvement in their studies comes from the use of a three-region boundary-layer structure, and they found that the majority of the scalings developed previously need to be modified by the inclusion of a $(1+\mathrm{Pr}^{-1/2})$ term to account for the additional Pr dependence. This improved approach has also been employed in a number of subsequent studies. For example, Bednarz *et al.* [22] used this approach to produce improved scalings for the transient thermomagnetic convection boundary layers of $\mathrm{Pr} > 1$ paramagnetic fluids in microgravity conditions; Aberra, Armfield, and Behnia [23] obtained improved scalings for steady-state natural-convection boundary layers for $\mathrm{Pr} > 1$ fluids under isoflux heating conditions; Xu, Patterson, and Lei [24] developed improved scalings for transient natural-convection boundary layers for $\mathrm{Pr} > 1$ fluids around a thin fin on the sidewall of a differentially heated cavity. More recently, Saha, Brown, and Gu [25] also employed the three-region boundary-layer structure to obtain improved scalings for the unsteady natural-convection boundary layer adjacent to a downward-facing inclined plate with uniform heat flux.

As demonstrated by Lin *et al.* [15] and Lin and Armfield [26], scalings which accurately predict the Pr variation have not been derived as yet for start-up and fully developed natural-convection boundary layers for $\mathrm{Pr} < 1$ fluids, and it is not clear at present whether such scalings exist. Nevertheless, our numerical simulation results, as presented in this study, show that the majority of the scalings obtained for $\mathrm{Pr} > 1$ fluids can be modified to predict the Pr variation for $\mathrm{Pr} < 1$ fluids, and unified Prandtl number scalings can be established for start-up and fully developed natural-convection boundary layers

for both $\mathrm{Pr} \gtrsim 1$ and $\mathrm{Pr} \lesssim 1$ fluids under isothermal heating conditions.

The remainder of this paper is organized as follows. The governing equations and the unified Prandtl number scalings that accommodate the Pr variation for both $\mathrm{Pr} \gtrsim 1$ and $\mathrm{Pr} \lesssim 1$ fluids under isothermal heating conditions are introduced in Sec. II. These scalings are validated and analyzed with a series of direct numerical simulation results with Pr varying in the range of $0.01 \leqslant \mathrm{Pr} \leqslant 100$ in Sec. III. Finally, conclusions are made in Sec. IV.

II. GOVERNING EQUATIONS AND UNIFIED PRANDTL NUMBER SCALINGS

A. Governing equations

Under consideration is the transient natural-convection boundary layer resulting from impulsively heating a quiescent isothermal Newtonian fluid by imposing a fixed higher temperature, T_w, on a vertical plate of height H. The fluid is initially at rest and at a uniform temperature T_0 ($T_0 < T_w$). It is assumed that the flow is laminar. Both $\mathrm{Pr} \gtrsim 1$ and $\mathrm{Pr} \lesssim 1$ fluids are considered.

The governing equations of motion are the Navier-Stokes equations with the Boussinesq approximation for buoyancy, which together with the temperature equation can be written in the following two-dimensional form:

$$\frac{\partial U}{\partial X} + \frac{\partial V}{\partial Y} = 0, \tag{1}$$

$$\frac{\partial U}{\partial t} + \frac{\partial (UU)}{\partial X} + \frac{\partial (VU)}{\partial Y} = -\frac{1}{\rho}\frac{\partial P}{\partial X} + \nu\left(\frac{\partial^2 U}{\partial X^2} + \frac{\partial^2 U}{\partial Y^2}\right), \tag{2}$$

$$\frac{\partial V}{\partial t} + \frac{\partial (UV)}{\partial X} + \frac{\partial (VV)}{\partial Y} = -\frac{1}{\rho}\frac{\partial P}{\partial Y} + \nu\left(\frac{\partial^2 V}{\partial X^2} + \frac{\partial^2 V}{\partial Y^2}\right) + g\beta(T - T_0), \tag{3}$$

$$\frac{\partial T}{\partial t} + \frac{\partial (UT)}{\partial X} + \frac{\partial (VT)}{\partial Y} = \kappa\left(\frac{\partial^2 T}{\partial X^2} + \frac{\partial^2 T}{\partial Y^2}\right), \tag{4}$$

where U and V are the horizontal (X direction) and vertical (Y direction) velocity components, t is time, P is pressure, T is temperature, g is the acceleration due to gravity, and β, ν, and κ are the thermal expansion coefficient, kinematic viscosity, and thermal diffusivity of fluid at the temperature T_0, respectively. Gravity acts in the negative Y direction.

For the transient natural-convection boundary-layer flow considered here, the major governing parameters are the Rayleigh number Ra and the Prandtl number Pr, defined as

$$\mathrm{Ra} = \frac{g\beta\Delta T H^3}{\nu\kappa}, \quad \mathrm{Pr} = \frac{\nu}{\kappa}, \tag{5}$$

where $\Delta T = T_w - T_0$.

The governing equations can be made dimensionless as follows:

$$\frac{\partial u}{\partial x} + \frac{\partial v}{\partial y} = 0, \tag{6}$$

$$\frac{\partial u}{\partial \tau} + \frac{\partial (uu)}{\partial x} + \frac{\partial (vu)}{\partial y} = -\frac{\partial p}{\partial x} + \frac{\mathrm{Pr}}{\mathrm{Ra}^{1/2}}\left(\frac{\partial^2 u}{\partial x^2} + \frac{\partial^2 u}{\partial y^2}\right), \tag{7}$$

$$\frac{\partial v}{\partial \tau} + \frac{\partial (uv)}{\partial x} + \frac{\partial (vv)}{\partial y} = -\frac{\partial p}{\partial y} + \frac{\mathrm{Pr}}{\mathrm{Ra}^{1/2}}\left(\frac{\partial^2 v}{\partial x^2} + \frac{\partial^2 v}{\partial y^2}\right) + \mathrm{Pr}\theta, \tag{8}$$

$$\frac{\partial \theta}{\partial \tau} + \frac{\partial (u\theta)}{\partial x} + \frac{\partial (v\theta)}{\partial y} = \frac{1}{\mathrm{Ra}^{1/2}}\left(\frac{\partial^2 \theta}{\partial x^2} + \frac{\partial^2 \theta}{\partial y^2}\right), \tag{9}$$

where x, y, u, v, τ, p, and θ are, respectively, the dimensionless forms of X, Y, U, V, t, P, and T, which are made dimensionless by their respective characteristic scales, i.e.,

$$x = \frac{X}{H}, \quad y = \frac{Y}{H}, \quad u = \frac{U}{V_0}, \quad v = \frac{V}{V_0}, \quad \tau = \frac{t}{(H/V_0)}, \quad p = \frac{P}{\rho V_0^2}, \quad \theta = \frac{T - T_0}{T_w - T_0}, \tag{10}$$

where $V_0 = \kappa \mathrm{Ra}^{1/2}/H$ is the characteristic velocity scale for natural-convection boundary layers (see, e.g., [8,13]). The origin of the coordinate system is located at the leading edge of the heated plate, at $x = 0$, $y = 0$.

B. Unified Prandtl number scalings

As demonstrated in [20,21], a three-region structure as shown in Fig. 1 can be depicted for the natural-convection boundary layers of $\mathrm{Pr} > 1$ fluids. The dominant parameters characterizing the flow behavior of a transient natural-convection boundary layer are the thickness of the thermal boundary layer, Δ_T, the thickness of the the outer viscous boundary layer, Δ_v, the thickness of the inner viscous boundary layer, Δ_{vi}, and the maximum vertical velocity within

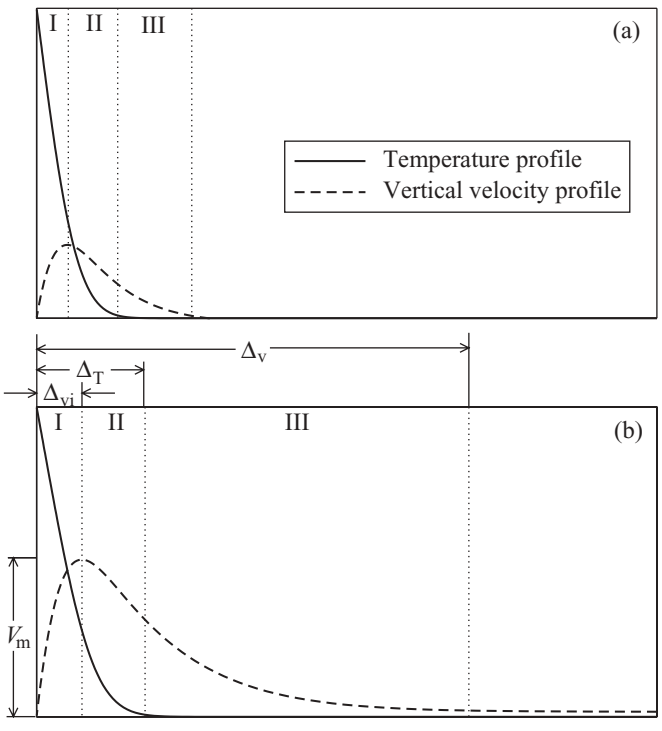

FIG. 1. Sketch of the horizontal profiles of temperature and vertical velocity at a specific height within a natural-convection boundary layer which depict a three-region structure: (a) at the start-up stage and (b) at the fully developed stage.

the viscous boundary layer, V_m. In this study, the dimensionless forms of these parameters are used, that is,

$$\delta_T = \frac{\Delta_T}{H}, \quad \delta_v = \frac{\Delta_v}{H}, \quad \delta_{vi} = \frac{\Delta_{vi}}{H}, \quad v_m = \frac{V_m}{V_0}. \tag{11}$$

For unsteady natural-convection boundary layers with $\mathrm{Pr} > 1$ fluids under isothermal heating conditions, the following was shown [20]:

During the transient, start-up stage,

$$\delta_T \sim \frac{\tau^{1/2}}{\mathrm{Ra}^{1/4}}, \tag{12}$$

$$\delta_v \sim \frac{\mathrm{Pr}^{1/2}\tau^{1/2}}{\mathrm{Ra}^{1/4}}, \tag{13}$$

$$\delta_{vi} \sim \frac{1}{(1+\mathrm{Pr}^{-1/2})}\frac{\tau^{1/2}}{\mathrm{Ra}^{1/4}}, \tag{14}$$

$$v_m \sim \frac{\tau}{(1+\mathrm{Pr}^{-1/2})^2}, \tag{15}$$

where δ_T, δ_v, δ_{vi}, and v_m are the dimensionless thermal boundary-layer thickness, the outer and inner viscous boundary-layer thickness, and the maximum vertical velocity within the viscous boundary layer at the start-up stage, respectively.

At the fully developed stage,

$$\tau_s \sim (1+\mathrm{Pr}^{-1/2})y^{1/2}, \tag{16}$$

$$\delta_{T,s} \sim \frac{\tau_s^{1/2}}{\mathrm{Ra}^{1/4}} \sim \frac{y^{1/4}}{\mathrm{Ra}^{1/4}}(1+\mathrm{Pr}^{-1/2})^{1/2}, \tag{17}$$

$$\delta_{v,s} \sim \frac{\mathrm{Pr}^{1/2}\tau_s^{1/2}}{\mathrm{Ra}^{1/4}} \sim \frac{y^{1/4}}{\mathrm{Ra}^{1/4}}\mathrm{Pr}^{1/2}(1+\mathrm{Pr}^{-1/2})^{1/2}, \tag{18}$$

$$\delta_{vi,s} \sim \frac{1}{(1+\mathrm{Pr}^{-1/2})}\frac{\tau_s^{1/2}}{\mathrm{Ra}^{1/4}} \sim \frac{y^{1/4}}{\mathrm{Ra}^{1/4}}\frac{1}{(1+\mathrm{Pr}^{-1/2})^{1/2}}, \tag{19}$$

$$v_{m,s} \sim \frac{\tau_s}{(1+\mathrm{Pr}^{-1/2})^2} \sim \frac{1}{(1+\mathrm{Pr}^{-1/2})}y^{1/2}, \tag{20}$$

where $\delta_{T,s}$, $\delta_{v,s}$, $\delta_{vi,s}$, and $v_{m,s}$ are the dimensionless thermal boundary-layer thickness, the outer and inner viscous boundary-layer thickness, and the maximum vertical velocity within the boundary layer at the fully developed stage, and τ_s is the dimensionless time scale for the boundary layer to attain the fully developed stage, respectively.

From the above scalings at the fully developed stage, it is seen that all parameters depend on Pr in the form of $(1+\mathrm{Pr}^{-1/2})^a$, where the index a is a constant and is different for different parameters (for τ_s, $a=1$; for $\delta_{T,s}$ and $\delta_{v,s}$, $a=\frac{1}{2}$; for $\delta_{vi,s}$, $a=-\frac{1}{2}$; and for $v_{m,s}$, $a=-1$).

We assume that for both $\mathrm{Pr} \gtrsim 1$ and $\mathrm{Pr} \lesssim 1$ fluids, the unified Prandtl number scalings for these parameters at the fully developed stage are also in the form of $(1+\mathrm{Pr}^{-1/2})^a$, that is, for the thermal boundary-layer thickness and the time scale for the development of the thermal boundary-layer thickness to attain the fully developed stage,

$$\tau_{T,s} \sim (1+\mathrm{Pr}^{-1/2})^{a_1} y^{1/2}, \tag{21}$$

$$\delta_{T,s} \sim \frac{\tau_{T,s}^{1/2}}{\mathrm{Ra}^{1/4}} \sim \frac{y^{1/4}}{\mathrm{Ra}^{1/4}}(1+\mathrm{Pr}^{1/2})^{a_1/2}; \tag{22}$$

for the inner viscous boundary-layer thickness and the time scale for the development of the inner viscous boundary-layer thickness to attain the fully developed stage,

$$\tau_{vi,s} \sim (1+\mathrm{Pr}^{-1/2})^{a_2} y^{1/2}, \tag{23}$$

$$\delta_{vi,s} \sim \frac{1}{(1+\mathrm{Pr}^{-1/2})}\frac{\tau_{vi,s}^{1/2}}{\mathrm{Ra}^{1/4}} \sim \frac{y^{1/4}}{\mathrm{Ra}^{1/4}}(1+\mathrm{Pr}^{-1/2})^{a_2/2-1}; \tag{24}$$

for the maximum vertical velocity and the time scale for the development of the maximum vertical velocity to attain the fully developed stage,

$$\tau_{m,s} \sim (1+\mathrm{Pr}^{-1/2})^{a_3} y^{1/2}, \tag{25}$$

$$v_{m,s} \sim \frac{\tau_{m,s}}{(1+\mathrm{Pr}^{-1/2})^2} \sim y^{1/2}(1+\mathrm{Pr}^{-1/2})^{a_3-2}. \tag{26}$$

In the above equations, a_1, a_2, and a_3 are constants whose values will be determined by the subsequent numerical simulation results.

As will be shown below, the numerical results demonstrate that the scalings for both $\mathrm{Pr} \gtrsim 1$ and $\mathrm{Pr} \lesssim 1$ fluids at the start-up stage are the same as those for $\mathrm{Pr} > 1$ fluids. The numerical results have also demonstrated that no unified Prandtl number scaling can be established for the outer viscous boundary-layer

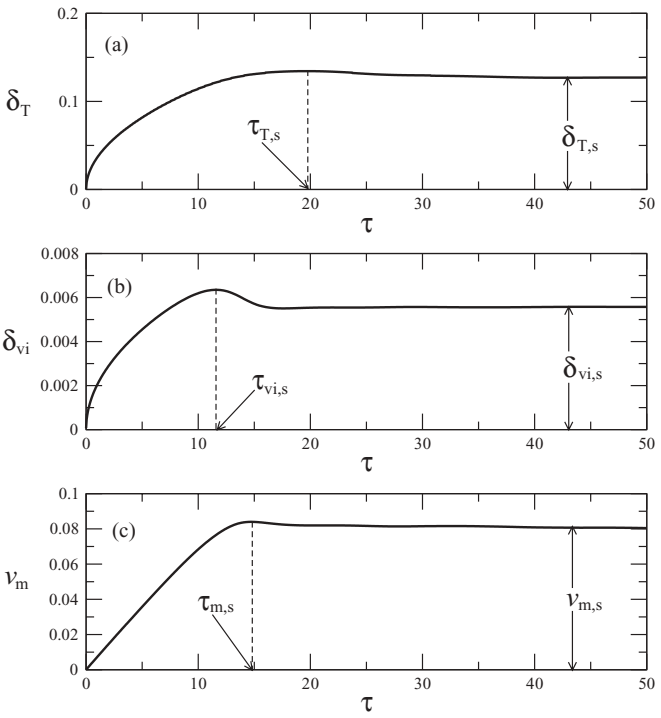

FIG. 2. Typical time series of (a) δ_T, the dimensionless thermal boundary-layer thickness; (b) δ_{vi}, the dimensionless inner viscous boundary-layer thickness; and (c) v_m, the dimensionless maximum vertical velocity within the viscous boundary layer, all at the height of $y = 0.5$ with $\mathrm{Pr} = 0.01$. $\delta_{T,s}$ is the dimensionless fully developed thermal boundary-layer thickness and $\tau_{T,s}$ is the dimensionless time for full development of δ_T; $\delta_{vi,s}$ is the dimensionless fully developed inner viscous boundary-layer thickness and $\tau_{vi,s}$ is the dimensionless time for full development of δ_{vi}; $v_{m,s}$ is the dimensionless fully developed maximum vertical velocity within the viscous boundary layer and $\tau_{m,s}$ is the dimensionless time for full development of v_m, respectively.

thickness ($\delta_{v,s}$) for both Pr $\gtrsim$ 1 and Pr $\lesssim$ 1 fluids, so no such unified Prandtl number scalings are included above for $\delta_{v,s}$ and $\tau_{v,s}$.

III. NUMERICAL RESULTS

As the Ra dependence of the scalings for natural-convection boundary layers has been thoroughly confirmed by numerous numerical results (see, e.g., [8–15]), this study focuses on the Pr and y dependence of the unified Prandtl number scalings obtained above. To do so, nine direct numerical simulations with Pr varying in the range of $0.01 \leqslant \mathrm{Pr} \leqslant 100$ (specifically Pr = 0.01, 0.05, 0.1, 0.5, 1, 5, 10, 50, and 100, respectively) were chosen, all at the same Rayleigh number $\mathrm{Ra} = 10^8$.

All the simulations were conducted in a two-dimensional rectangular computational domain having a dimensionless width 2 and a dimensionless height 1 with 493 × 397 nodes. To ensure the simulation results are accurate, a mesh dependency test has been conducted, and the details can be found in [20].

The typical time series of δ_T, δ_{vi}, and v_m at the height of $y = 0.5$ obtained from direct numerical simulation are presented in Fig. 2 for the specific case of Pr = 0.01. From this figure, it can be seen that the determination of the values of δ_T, δ_{vi}, and v_m at the fully developed stage from numerical results, i.e., $\delta_{T,s}$, $\delta_{vi,s}$, and $v_{m,s}$, is straightforward, as the values obtained, as indicated in the figure, are exactly what they represent. However, the determination of the times to signal the arrival of the fully developed stage for each parameter, i.e., the values of $\tau_{T,s}$, $\tau_{vi,s}$, and $\tau_{m,s}$, is not so straightforward, as no unique and consistent time can be found from the time series for the relevant parameter. Nevertheless, the time representing the end of the start-up stage on each time series, that is, the time at which the observed peak occurs, gives a unique and consistent value, which is believed to be the most appropriate numerically obtained time to represent the time to reach the fully developed stage for each parameter. Although this is not a perfect choice, as there is a transition period of time between the end of the start-up stage and the start of the fully developed stage, it is considered to be the best choice to represent the time to reach the fully developed stage. In this study, all numerically determined values of $\tau_{T,s}$, $\tau_{vi,s}$, and $\tau_{m,s}$ were obtained in this way.

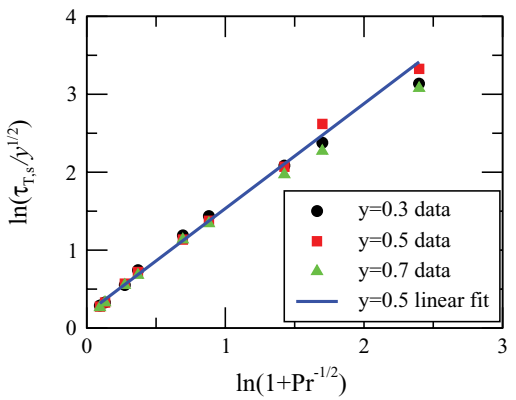

FIG. 3. (Color online) $\ln(\tau_{T,s}/y^{1/2})$ plotted against $\ln(1 + \mathrm{Pr}^{-1/2})$ at heights $y = 0.3$, 0.5, and 0.7, respectively, where $\tau_{T,s}$ is the dimensionless time scale for the development of the thermal boundary-layer thickness to attain the fully developed stage and Pr is the Prandtl number. The linear fit is obtained from the $y = 0.5$ data only.

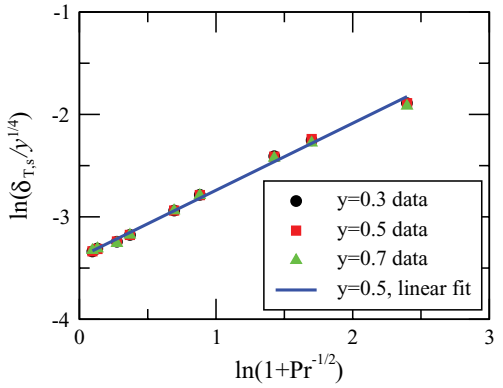

FIG. 4. (Color online) $\ln(\delta_{T,s}/y^{1/4})$ plotted against $\ln(1 + \mathrm{Pr}^{-1/2})$ at heights $y = 0.3$, 0.5, and 0.7, respectively, where $\delta_{T,s}$ is the dimensionless thermal boundary-layer thickness at the fully developed stage and Pr is the Prandtl number. The linear fit is obtained from the $y = 0.5$ data only.

First, the numerical results obtained for $\tau_{T,s}$ and $\delta_{T,s}$ with Pr in the range $0.01 \leqslant \mathrm{Pr} \leqslant 100$ are presented in scaled form in Figs. 3 and 4, respectively. In Fig. 3, $\tau_{T,s}$ scaled by $y^{1/2}$ is plotted against $(1 + \mathrm{Pr}^{-1/2})$ in log-log form. As can be seen, the results collapse approximately onto a single curve, confirming the scaling prediction $\tau_{T,s} \sim y^{1/2}$ as given in Eq. (21). Linear regression has been used to obtain the best linear fit to the data, giving

$$\ln(\tau_{T,s}/y^{1/2}) = 0.189 + 1.345 \ln(1 + \mathrm{Pr}^{-1/2}) \qquad (27)$$

with a regression constant of 0.9981. This gives the best-fit relation for $\tau_{T,s}$ as

$$\tau_{T,s} = 1.208(1 + \mathrm{Pr}^{-1/2})^{1.345} y^{1/2}. \qquad (28)$$

It is clear that the scaling relation $\tau_{T,s} \sim (1 + \mathrm{Pr}^{-1/2})^{1.345}$ gives an excellent representation of the dependence of $\tau_{T,s}$ on Pr for $0.01 \leqslant \mathrm{Pr} \leqslant 100$.

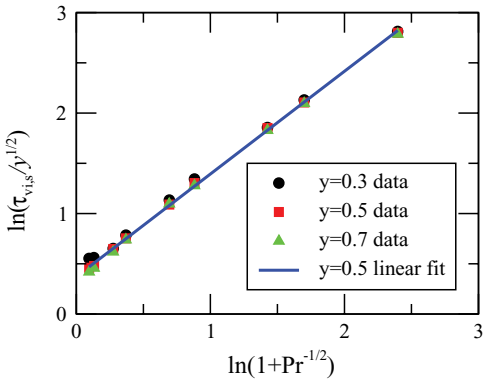

FIG. 5. (Color online) $\ln(\tau_{vi,s}/y^{1/2})$ plotted against $\ln(1 + \mathrm{Pr}^{-1/2})$ at heights $y = 0.3$, 0.5, and 0.7, respectively, where $\tau_{vi,s}$ is the dimensionless time scale for development of the inner viscous boundary-layer thickness to attain the fully developed stage and Pr is the Prandtl number. The linear fit is obtained from the $y = 0.5$ data only.

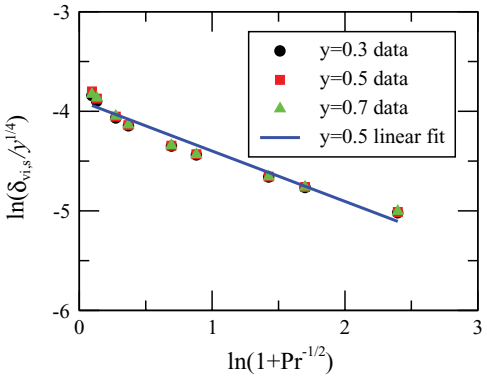

FIG. 6. (Color online) $\ln(\delta_{vi,s}/y^{1/4})$ plotted against $\ln(1+\mathrm{Pr}^{-1/2})$ at heights $y = 0.3$, 0.5, and 0.7, respectively, where $\delta_{vi,s}$ is the dimensionless inner viscous boundary-layer thickness at the fully developed stage and Pr is the Prandtl number. The linear fit is obtained from the $y = 0.5$ data only.

Similarly in Fig. 4, $\delta_{T,s}$ scaled by $y^{1/4}$ is plotted against $(1+\mathrm{Pr}^{-1/2})$ in log-log form, with the results supporting the scaling predictions given in Eq. (22). Linear regression gives the relation for $\delta_{T,s}$ as

$$\delta_{T,s} = 0.0336(1+\mathrm{Pr}^{-1/2})^{0.654} y^{1/4} \tag{29}$$

with a regression constant of 0.9976, demonstrating that the scaling relation $\delta_{T,s} \sim (1+\mathrm{Pr}^{-1/2})^{0.654}$ provides an excellent representation of the dependence of $\delta_{T,s}$ on Pr for $0.01 \leqslant \mathrm{Pr} \leqslant 100$.

Equation (28) shows that $a_1 = 1.345$ in the unified Prandtl number scaling for $\tau_{T,s}$ given in Eq. (21). Hence it is expected from the unified Prandtl number scaling for $\delta_{T,s}$, given in Eq. (22), that the index for this scaling should be $a_1/2 = 0.6725$. The numerical result in Eq. (29) gives 0.654 for the index, which is within 3.0% of the expected value of 0.6725. These results provide strong support for the unified Prandtl number scaling for $\delta_{T,s}$ for Pr in the range $0.01 \leqslant \mathrm{Pr} \leqslant 100$.

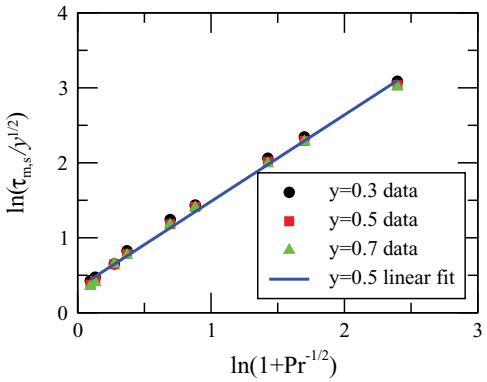

FIG. 7. (Color online) $\ln(\tau_{m,s}/y^{1/2})$ plotted against $\ln(1+\mathrm{Pr}^{-1/2})$ at heights $y = 0.3$, 0.5, and 0.7, respectively, where $\tau_{m,s}$ is the dimensionless time scale for the development of the maximum vertical velocity within the boundary layer to attain the fully developed stage and Pr is the Prandtl number. The linear fit is obtained from the $y = 0.5$ data only.

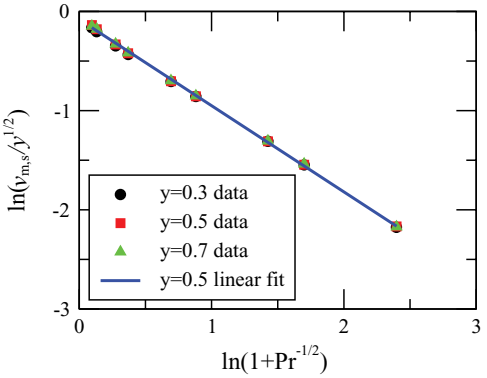

FIG. 8. (Color online) $\ln(v_{m,s}/y^{1/2})$ plotted against $\ln(1+\mathrm{Pr}^{-1/2})$ at heights $y = 0.3$, 0.5, and 0.7, respectively, where $v_{m,s}$ is the dimensionless maximum vertical velocity within the boundary layer at the fully developed stage and Pr is the Prandtl number. The linear fit is obtained from the $y = 0.5$ data only.

Secondly, the numerical results for $\tau_{vi,s}$ and $\delta_{vi,s}$ are plotted in scaled, log-log form in Figs. 5 and 6, respectively. Again the y dependencies predicted by Eqs. (23) and (24) for each of the quantities are supported by the collapse of all the results onto single curves in each of the figures. Linear regression was again used to obtain best-fit lines for each set of results,

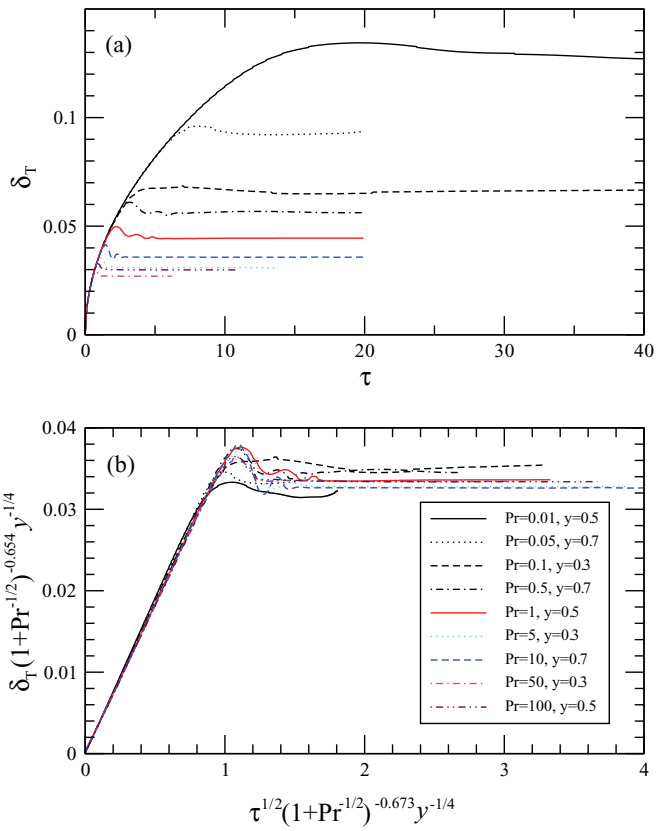

FIG. 9. (Color online) Time series of dimensionless thermal boundary-layer thickness (δ_T) for different Prandtl numbers (Pr) at various heights (y): (a) raw data and (b) δ_T scaled by $(1+\mathrm{Pr}^{-1/2})^{0.654} y^{1/4}$ plotted against $\tau^{1/2}$ where dimensionless time τ is scaled by $(1+\mathrm{Pr}^{-1/2})^{1.345} y^{1/2}$.

providing the following relations:

$$\tau_{vi,s} = 1.449(1 + \mathrm{Pr}^{-1/2})^{1.022} y^{1/2} \tag{30}$$

with a regression coefficient of 0.9997, and

$$\delta_{vi,s} = 0.0204(1 + \mathrm{Pr}^{-1/2})^{-0.506} y^{1/4} \tag{31}$$

with a regression coefficient of 0.9774. While the fit for $\tau_{vi,s}$ is again good, the fit for $\delta_{vi,s}$ is less satisfactory. This is also seen in Fig. 6, where it is evident that the fitted line deviates from the data in the small Pr region, suggesting that there is a further, weak, Pr dependence not captured by our scaling.

Equation (30) shows that $a_2 = 1.022$ in the scaling relation given in Eq. (23). Based on Eq. (24), the index for the $\delta_{vi,s}$ scaling should be $a_2/2 - 1 = -0.489$. The numerical result in Eq. (31) is -0.506, within 4% of the expected value, giving further support for the validity of the unified Prandtl number scaling given in Eq. (24).

Thirdly, the numerical results for $\tau_{m,s}$ and $v_{m,s}$ are presented in Figs. 7 and 8, respectively, in scaled and log-log form. All results again collapse onto single curves, supporting the $\tau_{m,s} \sim y^{1/2}$ and $v_{m,s} \sim y^{1/2}$ scalings given in Eqs. (25) and (26). Linear regression analysis gives the relations

$$\tau_{m,s} = 1.404(1 + \mathrm{Pr}^{-1/2})^{1.154} y^{1/2} \tag{32}$$

with a regression coefficient of 0.9985, and

$$v_{m,s} = 0.923(1 + \mathrm{Pr}^{-1/2})^{-0.869} y^{1/2} \tag{33}$$

with a regression coefficient of 0.9997.

In this case, Eq. (32) gives $a_3 = 1.154$, while Eq. (25) together with Eq. (26) imply that $a_3 - 2 = -0.846$. The numerical result in Eq. (33) is -0.869, which is within 3% of the expected value, again providing support for the unified Prandtl number scaling.

To further examine the validity of the scaling relations presented in the previous section, together with the empirical indices obtained above, the relations will be applied directly to numerically obtained time series and profile data. Figure 9 contains the time series of the thermal boundary-layer thickness δ_T for different Pr at various heights, in both raw and scaled form, using the scalings given in Eqs. (28) and (29), together with the $\delta_T \sim \tau^{1/2}$ scaling given in Eq. (12). It is observed that all the time series collapse onto a single straight line in the start-up stage (scaled $\tau < 1$). All scaled time series reach their individual maxima at almost the same time and then collapse onto approximately the same horizontal line, clearly demonstrating that the derived scaling relations together with the empirical indices provide good representations of the dependence of $\delta_{T,s}$ and $\tau_{T,s}$ on Pr over the Prandtl number range considered. Additionally, as the two indices 0.654 and 0.6725 are approximately equal, the scaling at start-up

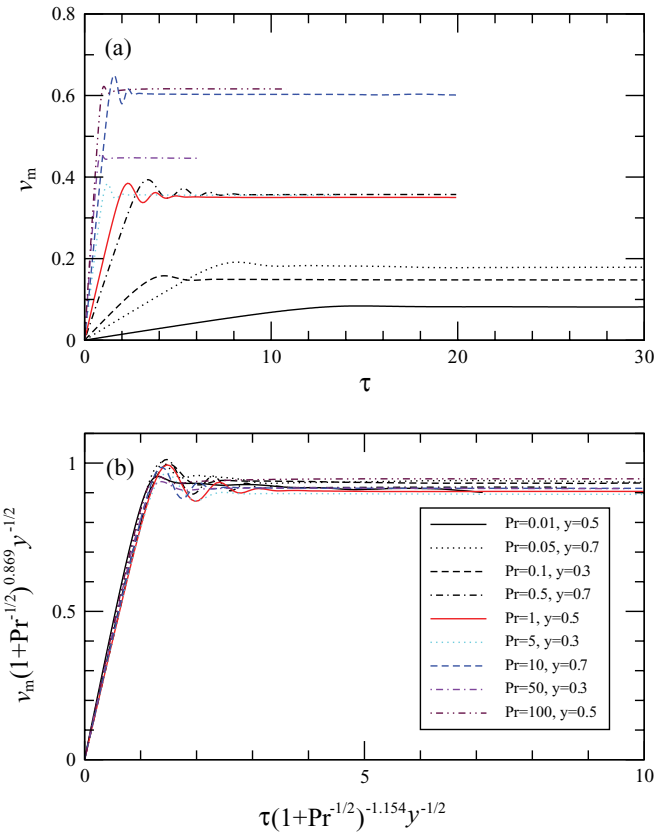

FIG. 10. (Color online) Time series of dimensionless maximum vertical velocity within the boundary layer (v_m) for different Prandtl numbers (Pr) at various heights (y): (a) raw data and (b) v_m scaled by $(1 + \mathrm{Pr}^{-1/2})^{-0.869} y^{1/2}$ plotted against dimensionless time τ which is scaled by $(1 + \mathrm{Pr}^{-1/2})^{1.154} y^{1/2}$.

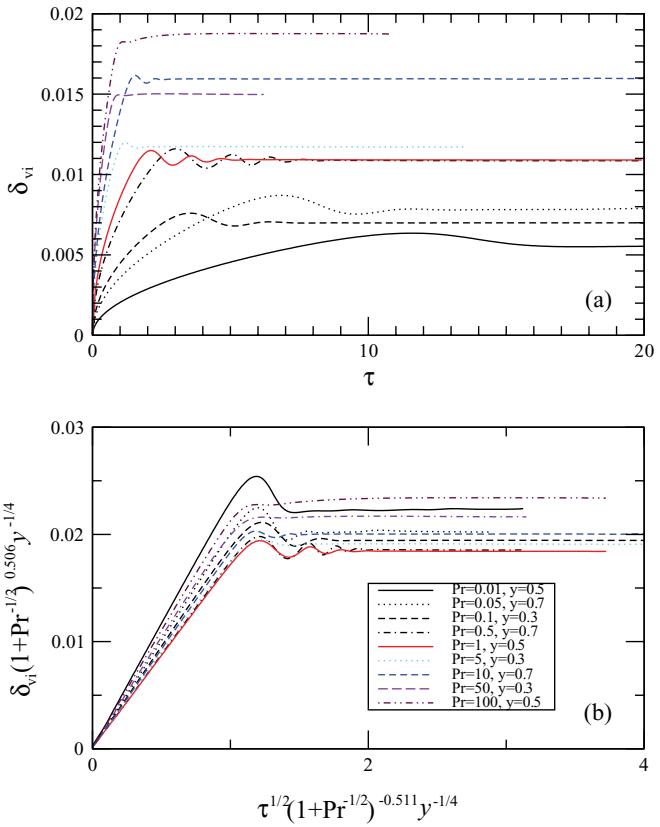

FIG. 11. (Color online) Time series of dimensionless inner viscous boundary-layer thickness (δ_{vi}) for different Prandtl numbers (Pr) at various heights (y): (a) raw data and (b) δ_{vi} scaled by $(1 + \mathrm{Pr}^{-1/2})^{-0.506} y^{1/4}$ plotted against $\tau^{1/2}$ where dimensionless time τ is scaled by $(1 + \mathrm{Pr}^{-1/2})^{1.022} y^{1/2}$.

reduces to $\delta_T \sim \tau^{1/2}$, the start-up scaling given in Eq. (12) and previously derived for Pr $>$ 1. It is evident that this start-up scaling may be applied to the full range of Pr considered here.

Figure 10 contains similar time-series results for v_m, using the scalings and indices given in Eqs. (32) and (33). Again the scalings bring all the results onto approximately the same curve, providing further validation of the scaling relations and empirical indices. It is also observed that dividing the τ-axis scaling by the v_m-axis scaling gives $v_m \sim \tau(1+\mathrm{Pr}^{-1/2})^{-2.023}$, which is very close to the start-up scaling derived for Pr $>$ 1, given in Eq. (15). It is apparent that this start-up scaling may also be applied to the full range of Pr considered here.

In Fig. 11, the scalings for δ_{vi} are examined, using the relations given in Eqs. (30) and (31), together with the relation $\delta_{vi} \sim \tau^{1/2}$ given in Eq. (14). It is observed that all the scaled time series become straight lines before attaining their individual maxima, validating the scaling $\delta_{vi} \sim \tau^{1/2}$, originally obtained for Pr $>$ 1, for the full Pr range considered. All scaled time series attain their individual maxima at almost the same time, validating the numerically obtained scaling given in Eq. (30). Although the scaling has considerably reduced the variation observed in the raw data, the scaled results have not been collapsed to a single curve, in either the start-up or fully developed phases of the flow, indicating that the scaling given in Eq. (31) does not provide a complete representation of the dependence of $\delta_{vi,s}$ on Pr. This is consistent with the poor linear fit of the numerical results as observed in Fig. 6.

The horizontal profiles of temperature at various heights during the start-up stage are presented in Fig. 12 for different Pr, in both raw and scaled form, with x scaled by $\tau^{1/2}$, as given in Eq. (12). It is seen in the raw data that the temperature profile during the start-up stage is independent of both Pr and y. The $x \sim \tau^{1/2}$ scaling collapses all the results onto a single curve, confirming that this scaling is appropriate for the full range of Prandtl numbers considered here during start-up. The equivalent temperature profiles at the fully developed stage, in raw and scaled form, are presented in Fig. 13, with x scaled by $(1+\mathrm{Pr}^{-1/2})^{0.654} y^{1/4}$, as given in Eq. (29). It is seen that this scaling provides a good representation of the width of the temperature profiles, bringing them all together in the outer region. However, the scaling does not provide such a good representation over the remainder of the profile, with considerable variation remaining in the region scaled $x < 0.025$, in contrast to the scaling for the start-up stage observed above.

Figure 14 shows the horizontal profiles of vertical velocity at various heights during the start-up stage for different Pr, in both raw and scaled form. In this case, x is scaled by $(1+\mathrm{Pr}^{-1/2})^{-1}\tau^{1/2}$, the scaling for δ_{vi} given in Eq. (14), and v is scaled by $(1+\mathrm{Pr}^{-1/2})^{-2}\tau$, the scaling for v_m given in Eq. (15). These scalings collapse all the results onto a single

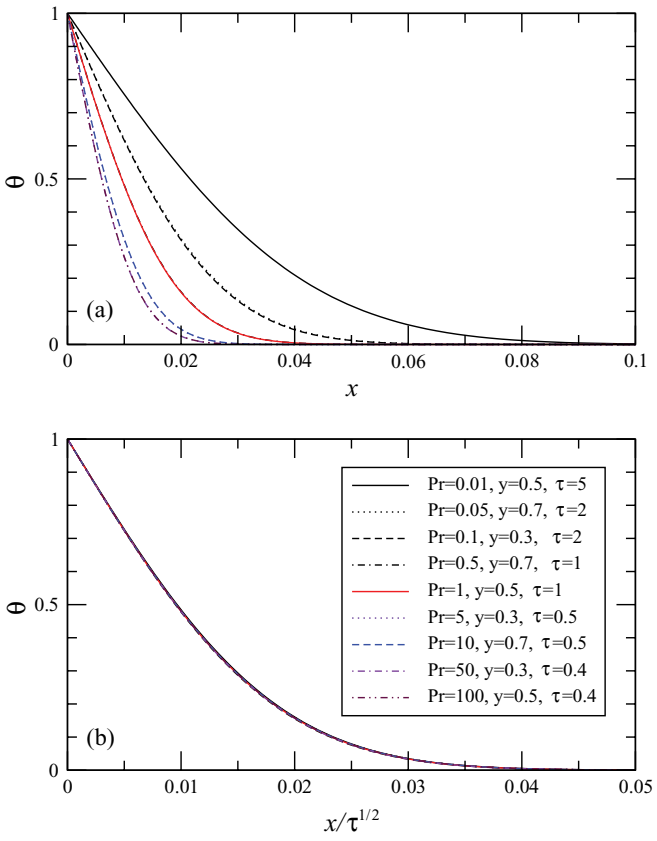

FIG. 12. (Color online) Horizontal profiles of dimensionless temperature (θ) for different Prandtl numbers (Pr) at various heights (y) at the start-up stage: (a) raw data and (b) θ plotted against $x/\tau^{1/2}$, where x is the horizontal coordinate.

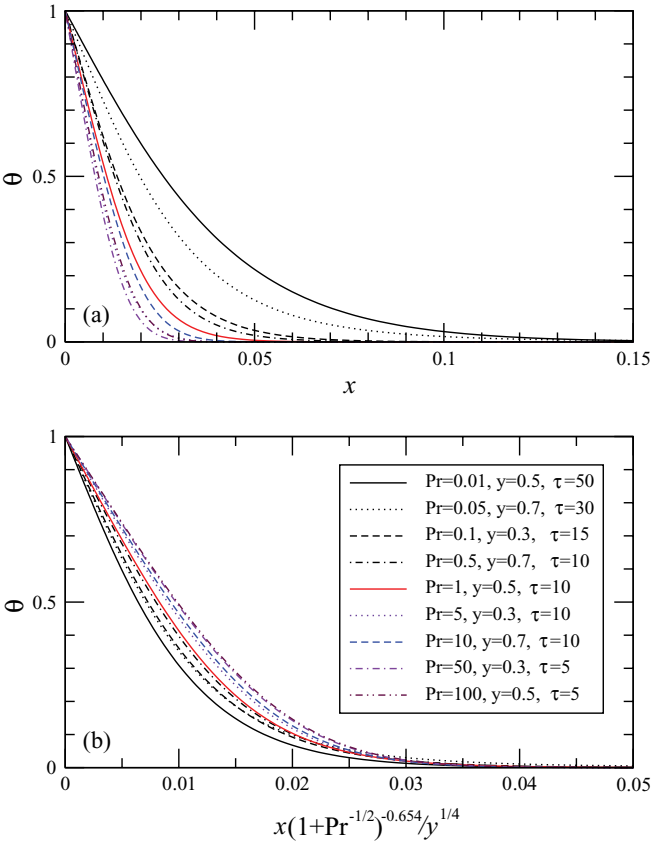

FIG. 13. (Color online) Horizontal profiles of dimensionless temperature (θ) for different Prandtl numbers (Pr) at various heights (y) at the fully developed stage: (a) raw data and (b) θ plotted against x scaled by $(1+\mathrm{Pr}^{-1/2})^{0.654} y^{1/4}$, where x is the horizontal coordinate.

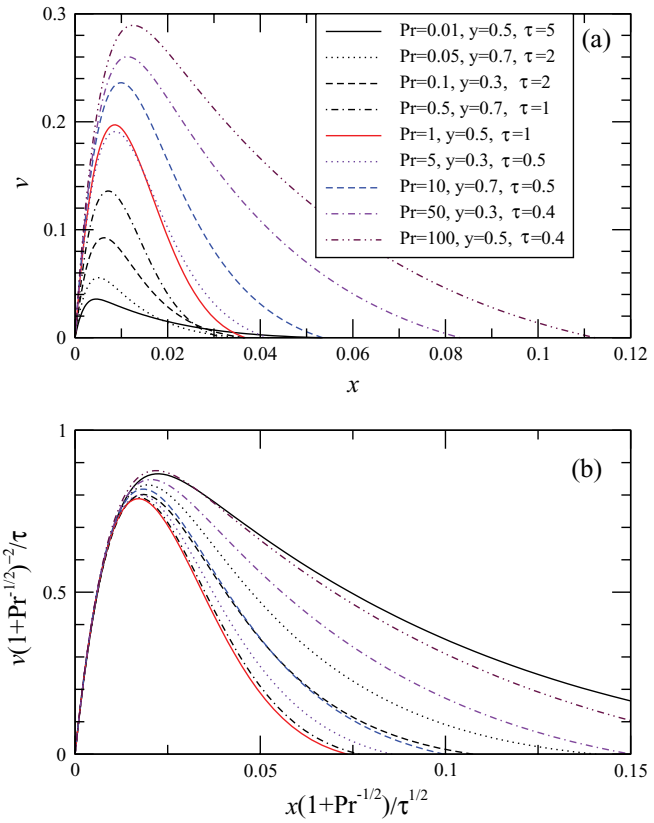

FIG. 14. (Color online) Horizontal profiles of vertical velocity (v) for different Prandtl numbers (Pr) at various heights (y) at the start-up stage: (a) raw data and (b) $v(1+\mathrm{Pr}^{-1/2})^{-2}/\tau$ plotted against $x(1+\mathrm{Pr}^{-1/2})/\tau^{1/2}$, where x is the horizontal coordinate.

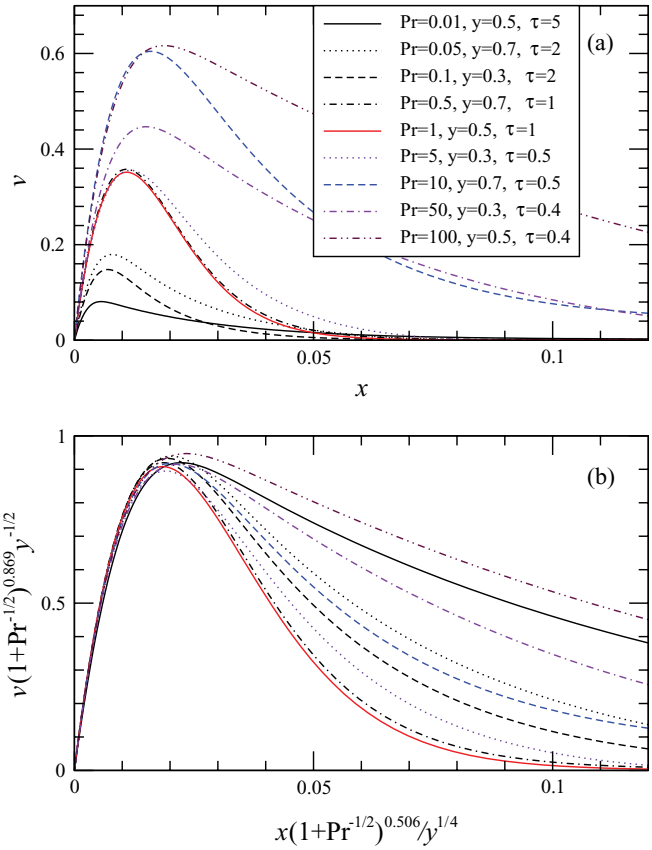

FIG. 15. (Color online) Horizontal profiles of vertical velocity (v) for different Prandtl numbers (Pr) at various heights (y) at fully developed stage: (a) raw data and (b) $v(1+\mathrm{Pr}^{-1/2})^{0.869}y^{-1/2}$ plotted against $x(1+\mathrm{Pr}^{-1/2})^{0.506}y^{-1/4}$, where x is the horizontal coordinate.

curve in the inner viscous boundary layer, the near-wall region, and bring all the maxima close to a single value, confirming their validity for the full range of Prandtl numbers considered here. The equivalent results for the vertical velocity at the fully developed stage are presented in Fig. 15 with x now scaled by $(1+\mathrm{Pr}^{-1/2})^{-0.506}y^{1/4}$ and v by $(1+\mathrm{Pr}^{-1/2})^{-0.869}y^{1/2}$, the dependencies of $\delta_{vi,s}$ and v_m on Pr as given in Eqs. (31) and (33). Once again it is seen that these scalings collapse all the profiles onto a single curve within the inner viscous boundary layer, scaled $x < 0.02$, and bring the maxima close to a single value, further validating these scalings for the fully developed stage of the flow.

A comparison of the times for transition to full development for the thermal boundary-layer thickness, $\tau_{T,s}$, inner viscous boundary-layer thickness, $\tau_{vi,s}$, and maximum velocity, $\tau_{m,s}$, is given in Table I. It can be seen that for the Pr > 1 results the times are similar, with $\tau_{T,s} < \tau_{vi,s}$. For the Pr $= 0.1$ result, the times are also similar, but with $\tau_{T,s} > \tau_{vi,s}$. Again for the Pr $= 0.01$ result, $\tau_{T,s} > \tau_{vi,s}$, but in this case by a much larger factor of 35%. For Pr $= 100$, 1, and 0.01, $\tau_{m,s}$ lies between $\tau_{T,s}$ and $\tau_{vi,s}$, while for Pr $= 10$, $\tau_{m,s} = \tau_{vi,s}$. It is noted that the times obtained here are for transition from start-up to fully developed flow, defined as the first peak in the time series, as described above and sketched in Fig. 2, rather than the times for an asymptotic approach to steady state which, due to the coupling of temperature and velocity, would be expected to be equal. The variation in the relation of $\tau_{T,s}$, $\tau_{vi,s}$, and $\tau_{m,s}$ with Pr is a further indication that different scaling relations must exist for each of these quantities, as observed above where different values of the index a were obtained, i.e., a_1 for $\tau_{T,s}$, a_2 for $\tau_{vi,s}$, and a_3 for $\tau_{m,s}$.

IV. CONCLUSIONS

From the above results and analysis, it is clear that the scalings developed for the transient natural-convection boundary layers for Pr > 1 fluids under isothermal heating conditions can be extended to Pr $\lesssim 1$ fluids to provide unified Prandtl number scalings for the transient natural-convection boundary layers for both Pr $\gtrsim 1$ and Pr $\lesssim 1$ fluids. The direct numerical simulation results with Pr varying in the range

TABLE I. Numerical results for $\tau_{T,s}$, $\tau_{vi,s}$, and $\tau_{m,s}$ at height $y = 0.5$ and $\mathrm{Ra} = 10^8$ for different values of Pr.

Pr	$\tau_{T,s}$	$\tau_{vi,s}$	$\tau_{m,s}$
100	0.93	1.12	1.03
10	1.25	1.35	1.35
1	2.20	2.10	2.30
0.1	5.61	4.50	5.31
0.01	19.67	11.61	14.72

$0.01 \leqslant \mathrm{Pr} \leqslant 100$ show that at the start-up stage, the Prandtl number scalings for the major parameters characterizing natural-convection boundary-layer behavior, i.e., the thermal boundary-layer thickness, inner viscous boundary-layer thickness, and maximum vertical velocity within the viscous boundary layer, are the same as those for $\mathrm{Pr} > 1$ fluids. At the fully developed stage, however, all these parameters depend on Pr in the form $\sim(1 + \mathrm{Pr}^{-1/2})^a$, where the index a is a constant that is different for each parameter. Unified Prandtl number scalings for both $\mathrm{Pr} \gtrsim 1$ and $\mathrm{Pr} \lesssim 1$ fluids can then be obtained by just modifying the value of a for each parameter. The developed unified Prandtl number scalings are shown in general to provide an accurate prediction of the Pr variation for both $\mathrm{Pr} \gtrsim 1$ and $\mathrm{Pr} \lesssim 1$ fluids.

ACKNOWLEDGMENTS

The support from the National Natural Science Foundation of China (Grant No. 11072211), the Program for Changjiang Scholars and Innovative Research Team in University of Ministry of Education of China, and the Australian Research Council is gratefully acknowledged.

[1] I. Catton, *Proceedings of the Sixth International Heat Transfer Conference*, Vol. 6, Toronto, 1978, p. 13.
[2] S. Ostrach, *Proceedings of the Seventh International Heat Transfer Conference*, Vol. 1, Munich, 1982, p. 365.
[3] B. Gebhart, Y. Jaluria, R. L. Mahajan, and B. Sammakia, *Buoyancy-Induced Flows and Transport* (Hemisphere, New York, 1988).
[4] J. M. Hyun, Adv. Heat Transf. **24**, 277 (1994).
[5] R. J. Goldstein *et al.*, Int. J. Heat Mass Transf. **48**, 819 (2005).
[6] T. M. Shil, C. Thamire, C. H. Sung, and A. L. Ren, Numer. Heat Transf., Pt. A **57**, 159 (2010).
[7] T. M. Shil, M. Arie, and D. Ko, Numer. Heat Transf., Pt. A **60**, 883 (2011).
[8] J. C. Patterson and J. Imberger, J. Fluid Mech. **100**, 65 (1980).
[9] W. Lin and S. W. Armfield, Int. J. Heat Mass Transf. **42**, 4117 (1999).
[10] W. Lin and S. W. Armfield, Int. J. Heat Fluid Flow **22**, 72 (2001).
[11] I. Lira, Eur. J. Phys. **29**, 1301 (2008).
[12] W. Lin and S. W. Armfield, Phys. Rev. E **72**, 016306 (2005).
[13] W. Lin, S. W. Armfield, and J. C. Patterson, J. Fluid Mech. **574**, 85 (2007).
[14] S. W. Armfield, J. C. Patterson, and W. Lin, Int. J. Heat Mass Transf. **50**, 1592 (2007).
[15] W. Lin, S. W. Armfield, and J. C. Patterson, Int. J. Heat Mass Transf. **51**, 327 (2008).
[16] P. A. Kottke, T. P. Ferguson, and A. G. Fedorov, J. Heat Transf. **126**, 250 (2004).
[17] Z. Alloui, P. Vasseur, and M. Reggio, Heat Mass Transf. **48**, 627 (2012).
[18] S. C. Saha and M. M. K. Khan, Int. J. Heat Mass Transf. **55**, 2268 (2012).
[19] M. Capobianchi and A. Aziz, Int. J. Thermal Sci. **54**, 82 (2012).
[20] W. Lin, S. W. Armfield, J. C. Patterson, and C. Lei, Phys. Rev. E **79**, 066313 (2009).
[21] J. C. Patterson, C. Lei, S. W. Armfield, and W. Lin, Int. J. Thermal Sci. **48**, 1843 (2009).
[22] T. P. Bednarz, W. Lin, J. C. Patterson, C. Lei, and S. W. Armfield, Int. J. Heat Fluid Flow **30**, 1157 (2009).
[23] T. Aberra, S. W. Armfield, and M. Behnia, *Proceedings of the International Symposium on Advances in Computational Heat Transfer (CHT-08)*, Vol. 13, Marrakech, Morocco, 2008, p. 363.
[24] F. Xu, J. C. Patterson, and C. Lei, J. Fluid Mech. **639**, 261 (2009).
[25] S. C. Saha, R. J. Brown, and Y. T. Gu, Int. J. Heat Mass Transf. **55**, 2394 (2012).
[26] W. Lin and S. W. Armfield, Phys. Rev. E **72**, 066309 (2005).